Accuracy of Approximate Inversion Schemes in Quantitative Photacoustic Imaging

Roman Hochuli, Paul C. Beard and Ben Cox

Department of Medical Physics & Bioengineering, University College London, UK.

ABSTRACT

Five numerical phantoms were developed to investigate the accuracy of approximate inversion schemes in the reconstruction of oxygen saturation in photoacoustic imaging. In particular, two types of inversion are considered: *Type I*, an inversion that assumes fluence is unchanged between illumination wavelengths, and *Type II*, a method that assumes known background absorption and scattering coefficients to partially correct for the fluence. These approaches are tested in tomography (PAT) and acoustic-resolution microscopy mode (AR-PAM). They are found to produce accurate values of oxygen saturation in a blood vessel of interest at shallow depth - less than 3mm for PAT and less than 1mm for AR-PAM.

Keywords: Photoacoustic imaging, Quantitative inversion, Fluence correction, Oxygen saturation

1. INTRODUCTION

Photoacoustic imaging (PAI) is a technique that provides high sensitivity through spectrally-dependent absorption of near-infrared light by different tissue types and high resolution by the relatively low scattering experienced by acoustic waves. The optical forward problem describes the formation of the initial acoustic pressure distribution through the absorption of the light fluence, to form the absorbed energy density, and the subsequent thermalisation of the absorbed energy and increase in pressure, characterised by the Grüneisen parameter. The acoustic forward problem consists of the propagation of the initial pressure distribution to a detection surface. There are therefore two sequential inversions within PAI: acoustical and optical. The acoustic inversion is required to reconstruct the initial acoustic pressure distribution. The initial acoustic pressure is related to three spatially-variant, unknown parameters: the Grüneisen parameter, the light fluence and the absorption coefficient. Hence, photoacoustic images are not proportional to the absorption coefficient and a further inversion step is required to account for the unknown fluence distribution. This would allow for reconstruction of physiologically relevant quantities, such as a chromophore concentrations or oxygen saturation - a ratio of oxygenated haemoglobin concentration, c_{HbO2}, to total haemoglobin concentration, c_{HbT}, $sO_2 = \frac{c_{HbO2}}{c_{HbT}}$. Assuming perfect reconstruction of the initial pressure distribution, there are two key issues that afflict the recovery of chromophore concentrations, which are made explicit by considering the optical forward problem (1).

$$p_0(\lambda, \mathbf{x}) = \Gamma \Phi(\lambda, \mathbf{x}; c_k, \mu_s, g) \sum_{k=1}^{K} \alpha_k(\lambda) c_k(\mathbf{x}), \tag{1}$$

where p_0 is the initial acoustic pressure distribution, Γ is the Grüneisen parameter, Φ is the light fluence, α_k is the molar absorption coefficient for the k^{th} chromophore, c_k is the concentration of the k^{th} chromophore, λ is the wavelength of the light fluence, $\mathbf{x}$ is position, μ_s is the scattering coefficient and g is the anisotropy factor.

Equation (1) demonstrates that Φ is itself a function of the quantity of interest - c_k - and the fluence is typically not known within the tissue. The dependence of the fluence on the chromophore concentrations and the scattering coefficient means that it is also spectrally-dependent, resulting in 'spectral colouring' of the fluence. Furthermore, the fluence varies depending on position within the medium, referred to as 'spatial corruption' of the fluence. These two features make the recovery c_k or oxygen saturation, sO_2, when performing multiwavelength imaging of blood, non-trivial.

Send correspondence to: r.hochuli@ucl.ac.uk

Photons Plus Ultrasound: Imaging and Sensing 2014, edited by Alexander A. Oraevsky, Lihong V. Wang,
Proc. of SPIE Vol. 8943, 89435V · © 2014 SPIE · CCC code: 1605-7422/14/$18 · doi: 10.1117/12.2039825

Several techniques have been proposed in the literature to ameliorate the effect of fluence heterogeneity in this inverse problem, such as approximations stating wavelength independence of the fluence,[1–3] analytical solutions to the diffusion equation,[4] or explicitly modelling the light field using numerical simulations.[5,6]

The latter makes minimal *a priori* assumptions about the fluence distribution and requires an iterative method to estimate the absorption coefficient in conjunction with a finite element implementation of the diffusion approximation[1,7,8] or the radiative transport equation.[6,9] However, such implementations are highly computationally intensive, and are currently impractical to apply in practice due to the large-scale nature of the inversion and large uncertainties involved in modelling an experimental setup.

There are few studies that systematically and rigorously test the circumstances under which approximate fluence correction methods are valid in known and realistic phantoms. Moreover, certain approximations may yield accurate results in certain scenarios, while they may not be accurate in other situations.

In this study we demonstrate the region of validity of two approximate inversion schemes in certain conditions through the consideration of five numerical experiments. In particular, this paper begins by introducing two types of approximate inversion scheme and applies them to the reconstruction of sO_2 in five numerical mouse brain phantoms. The five phantoms were designed to have increasingly complex properties; these included spectrally-dependent background tissue, the amount of vasculature present in the background and a skin layer surrounding the brain. The increasingly realistic nature of the phantoms allows us to better test the inversion algorithms proposed in Section 3 and determine the conditions in which they are valid.

2. DEVELOPMENT OF A NUMERICAL PHANTOM

A 3D μCT image of mouse brain vascular cast, shown in Figure 1(a), was used as a basis for constructing the five phantoms. The original 2.5μm isotropic resolution dataset was compressed to 25μm isotropic resolution in Amira (Visualization Sciences Group, FEI). The data was loaded into MATLAB in order to rotate the dataset so that the z-axis passed through the centre of the brain and to threshold the brain from the background (Figure 1(b)). A vessel of interest was then segmented from background brain tissue using connected-component analysis and thresholding based on component length, allowing the largest component to be selected; properties could then be separately attributed to the vessel of interest and to background brain tissue. A total haemoglobin concentration in the vessel of interest of 150gl^{-1} was assumed and five different backgrounds were chosen, which are summarised below.

The five cases below involve two broad background absorption types: spectrally-dependent and spectrally-independent. In the spectrally-independent cases, the background has a single absorption coefficient for all wavelengths. The value chosen for this is similar to brain tissue illuminated at 800nm. In the spectrally-independent case, we assume a total haemoglobin concentration of the background, $c_{HbT}^{bg} = 5.63\text{gl}^{-1}$, as well as an oxygenation value of $sO_2 = 60.7\%$ - both realistic values for brain tissue.[10]

Case (a) Homogeneous, spectrally-uniform background with $\mu_a^{bg} = 0.03\text{mm}^{-1}$.

Case (b) Homogeneous, blood-filled background with $c_{HbT}^{bg} = 5.63\text{gl}^{-1}$ and $sO_2 = 60.7\%$.

Case (c) Heterogeneous, spectrally-uniform background with $\mu_a^{bg} = 0.03\text{mm}^{-1}$. Background vasculature was given the same properties as the vessel of interest.

Case (d) Heterogeneous, blood-filled background with $c_{HbT}^{bg} = 5.63\text{gl}^{-1}$ and $sO_2 = 60.7\%$. Background vasculature was given the same properties as the vessel of interest.

Case (e) Heterogeneous, blood-filled background with $c_{HbT}^{bg} = 5.63\text{gl}^{-1}$ and $sO_2 = 60.7\%$. Background vasculature was given the same properties as the vessel of interest. Variable thickness skin layer surrounding the brain having $c_{HbT}^{skin} = 0.48\text{gl}^{-1}$ at 98% oxygenation and 0.87gl^{-1} eumelanin concentration.

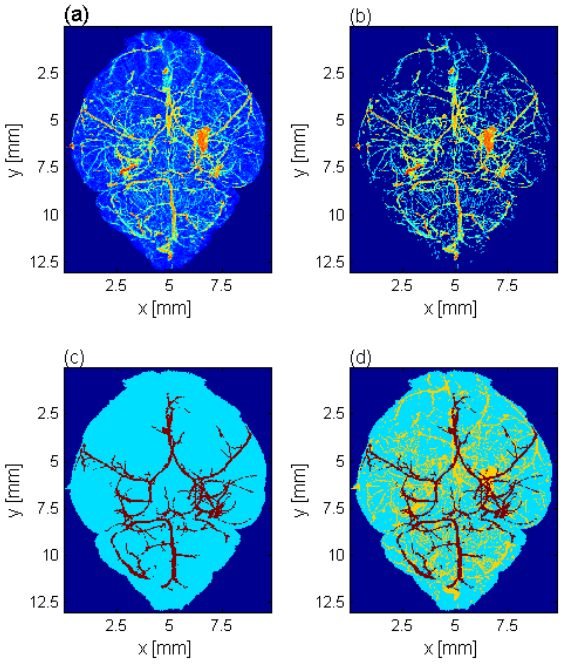

Figure 1. (a) Maximum intensity projection (MIP) in z-direction of μCT image of mouse brain vascular cast; (b) MIP in z-direction of thresholded μCT image of mouse brain vascular cast showing vasculature; (c) MIP in z-direction of vessel of interest labelled in red and background in blue; (d) MIP in z-direction of vessel of interest labelled in red, background vasculature in yellow background in blue.

A homogeneous scattering coefficient was used, the value of which was similar to that of human brain tissue, and varied as a function of wavelength according to $\mu_s' = A\left(\frac{\lambda}{500nm}\right)^{-B}$.[10] The anisotropy factor was heterogeneously distributed with $g = 0.9$ for the tissue background and $g = 0.9945$ for blood vessels.

Cases (a) and (b) correspond to Figure 1(c), while Cases (c)-(e) are represented in Figure 1(d).

3. TYPES OF INVERSION SCHEME

Two types of approximate inversion scheme that might be used to tackle this problem, categorised according to the degree to which assumptions are made about the fluence distribution, are discussed in detail below.

Type I - *Unchanged fluence.* *Type I* inversions assume that the fluence distribution at the excitation wavelengths are equal.

Example *Type I* linear inversion: in the case of a two-wavelength (λ_1, λ_2) inversion to recover oxygen saturation, the optical forward problem can be written as a simple linear system

$$\begin{bmatrix} p_0(\lambda_1, \mathbf{x}) \\ p_0(\lambda_2, \mathbf{x}) \end{bmatrix} = \Gamma \begin{bmatrix} \alpha_{HbO2}(\lambda_1) & \alpha_{Hb}(\lambda_1) \\ \alpha_{HbO2}(\lambda_2) & \alpha_{Hb}(\lambda_2) \end{bmatrix} \begin{bmatrix} \Phi(\lambda_1, \mathbf{x}) c_{HbO2}(\mathbf{x}) \\ \Phi(\lambda_2, \mathbf{x}) c_{Hb}(\mathbf{x}) \end{bmatrix}. \tag{2}$$

Pre-multiplying both sides by the inverse of the matrix of molar absorption coefficients provides an expression for the oxy- and deoxy-haemoglobin concentrations encoded by the fluence at wavelengths at λ_1 and λ_2, respectively. Computing the oxygen saturation as

$$sO_2(\mathbf{x}) = \frac{\Phi(\lambda_1, \mathbf{x}) c_{HbO2}(\mathbf{x})}{\Phi(\lambda_1, \mathbf{x}) c_{HbO2}(\mathbf{x}) + \Phi(\lambda_2, \mathbf{x}) c_{Hb}(\mathbf{x})} \tag{3}$$

under the assumption that $\Phi(\lambda_1) \approx \Phi(\lambda_2)$ gives the desired quantity: $sO_2(\mathbf{x}) = \frac{c_{HbO2}}{c_{HbO2}+c_{Hb}}$.

Example *Type I* nonlinear inversion: in the presence of a dynamic change from oxygenation state a to state b in a vessel of interest, it is assumed that the ratio of the photoacoustic amplitudes at points within the vessel, at each oxygenation state and a single illumination wavelength, λ_n, will be independent of the fluence.[3] This is expressed in Equation (4).

$$\frac{p_0(\lambda_n, sO_2(a))}{p_0(\lambda_n, sO_2(b))} = \frac{c_{HbT}(a)}{c_{HbT}(b)} \frac{\left[sO_2(a)\alpha_{HbO2}(\lambda_n) + (1 - sO_2(a))\alpha_{Hb}(\lambda_n)\right] \Phi(\lambda_n, sO_2(a))}{\left[sO_2(b)\alpha_{HbO2}(\lambda_n) + (1 - sO_2(b))\alpha_{Hb}(\lambda_n)\right] \Phi(\lambda_n, sO_2(b))} \tag{4}$$

In order to reconstruct the three independent parameters in the equation above ($c_{HbT}(a)/c_{HbT}(b)$, $sO_2(a)$, $sO_2(b)$), at least three illumination wavelengths are required in conjunction with the assumption that $\Phi(\lambda_n, sO_2(a)) = \Phi(\lambda_n, sO_2(b))$. A nonlinear optimisation is then used to perform a least-squares minimisation between the ratio of measured signals, $\frac{p_0^{\text{meas}}(\lambda_n, sO_2(a))}{p_0^{\text{meas}}(\lambda_n, sO_2(b))}$, and the right-hand side of Equation (4). This approach has two significant advantages; first, it is made independent of the Grüneisen parameter, which is typically unknown in practice, as it cancels in Equation (4). Second, it relies on the fluence at a single wavelength and two oxygenation states being equal, rather than in the linear inversion method which requires the fluence to be equal at two *different* wavelengths. Under the assumption that the background undergoes no change in oxygenation when vascular oxygenation changes, the background absorption coefficient remains unchanged, resulting in less spectral colouring of the fluence compared with the spectral distortion present when performing a linear inversion.

Type II - Correction for background fluence. Unlike *Type I* methods, this approach does not assume the wavelength is unchanged between illumination wavelengths and partially corrects for the spatial corruption and spectral colouring of the fluence by using prior knowledge of the background optical properties. This relies on the assumption that fluence is not significantly changed by features in the foreground (i.e. those that have different optical properties to the background) and the background absorption and scattering dominate in terms of their effect on the fluence. Such analytic approaches are attractive due to their limited computational burden and ease of implementation. For instance, a 1D exponential correction can be applied to the data provided the source region is much larger than the region of interest, the source is collimated, and that the background absorption and/or scattering are known.

Example *Type II* linear inversion: this method assumes a known background absorption coefficient which has a dominant impact on the fluence relative to the vasculature. This can be justified by considering that, despite the vasculature having a higher absorption coefficient at the excitation wavelengths, it occupies a smaller volume within the domain. In such circumstances, the use of a 1D analytic model for the fluence, known as the Beer-Lambert Law, may be suitable given the qualifications above. For illumination along the z-axis,

$$\Phi(\lambda, z) = \exp(-\mu_a^{bg}(\lambda) z), \tag{5}$$

where μ_a^{bg} is the homogeneous background absorption coefficient and z is the distance along the z-axis from the domain's surface to a point of interest.

By assuming this fluence model, measured data, $p_0^{\text{meas}}(\lambda, \mathbf{x})$, can be partially corrected by dividing by the 1D fluence model: $p_0^{\text{corr}}(\lambda, \mathbf{x}) = \frac{p_0^{\text{meas}}}{\Phi(\lambda, z)}$. $p_0^{\text{corr}}(\lambda, \mathbf{x})$ can then be inverted using the linear inversion illustrated in Equation (2) to reconstruct sO_2.

4. TESTING THE ACCURACY OF APPROXIMATE INVERSION SCHEMES

In this section we consider the application of two types of approximate inversion scheme and test their accuracy in reconstructing sO_2 in a numerical mouse brain phantom, in both tomography and acoustic-resolution microscopy mode.

4.1 Photoacoustic Tomography

Numerical experiments were carried out using wide-field, collimated illumination with 10mm beam-width at 780nm and 820nm. MCX[11] Monte Carlo (MC) code was used to simulate the fluence, which was then used to compute the initial pressure distribution, $p_0^{\text{meas}}(\lambda, \mathbf{x})$, assuming $\Gamma = 1$ and ideal acoustic reconstruction (i.e. no limited-view artefacts and broadband acoustic detectors). A MC model, rather than a diffusion model of light transport, was used to ensure accurate representation of the light field near the source, as this region is of interest in many applications.

However, MC models exhibit some level of noise which depends on the size of the domain, voxel size and whether the illumination is focused. It is therefore important to quantify the level of noise in the simulations run for these experiments, which were run for 10^9 photons. This was achieved by running five simulations, at a single wavelength, in the phantom employed in this study and calculating the ratio of the standard deviation to the mean (coefficient of variation, CV) for the fluence in a given voxel; this was performed on 10^6 randomly selected voxels throughout the domain for simulations in which 10^5, 10^6, 10^7 and 10^8 photons were simulated.

The CV values generated from this analysis reflect the deviation of the fluence relative to its expected value, for a given domain and number of photons. As such, it is expected that both the mean and standard deviation of the CV values decreases with increasing number of photons. This was indeed observed; however, the standard deviation of the CV values as a function of number of photons, i.e. the inter-voxel variability of the uncertainty in the fluence, remained at nearly 5% while the mean was 6% for 10^8 photons, giving a maximum uncertainty of 11%. Thus, for simulations of 10^9 photons, we anticipate the maximum possible error in the fluence to be approximately 6%, by extrapolating the CV values as a function of number of photons simulated. Error propagation to compute the maximum possible error in estimated sO_2 demonstrates that $\frac{\delta sO_2}{sO_2} \propto \frac{\delta\phi}{\phi}$, where the δ is used to indicate the uncertainty in the relevant value. As such, the maximum percentage error in sO_2 is *at most* 6%.

The *Type I* and *Type II* inversions were applied to each of the five cases described in Section 2 for vessel oxygenation values of 70%, 80%, 90% and 100% and the % error in sO_2 at each point in the vessel of interest was calculated. However, it was found that the % errors exhibited large point-to-point variability due to the fluence variability described above. Therefore, the percent error in reconstructed sO_2 in the vessel of interest was averaged transversely over each slice (thickness 0.025mm) to produce the average vessel oxygenation at that depth. The average percent error in vessel oxygenation, Δ, and the one-σ range, the mean plus-or-minus the standard deviation of the percent error in sO_2, was calculated. These two quantities were then plotted as a function of depth for each case, as shown in Figure 2 for 90% vessel oxygenation.

Presenting the data in this way is effective as it reduces the point-wise variation of the fluence due to MC noise. There is a risk that applying averaging in this manner could introduce a reduction in the impact of the spatial corruption of the fluence. However, the choice to average sO_2 over a slice mostly preserves the spatial corruption of the fluence along the depth direction as the gradient of the fluence in a narrow region is typically greater in the z-direction than in the transverse directions for wide-field illumination (however this may only apply for illumination wavelengths where the absorption coefficients are similar and the scattering coefficients are similar). This allows us to better investigate the effect of spatial corruption and spectral colouring of the fluence on sO_2 estimation.

This means that, for the two quantities plotted below, Δ is representative of how accurately oxygen saturation in the vessel can be recovered at a particular depth, whilst the one-σ range represents both the fluence corruption and the MC noise within a given transverse slice. It was shown above that the maximum possible error in sO_2 due to MC noise is 6%; as this is comprised within the one-σ range in the data in Figure 2, it is not shown.

In Case (a), where the background is homogeneous and spectrally-independent, the linear inversion performs well, reconstructing oxygen saturation to within 10% accuracy at depths up to 6mm, with accuracy of the

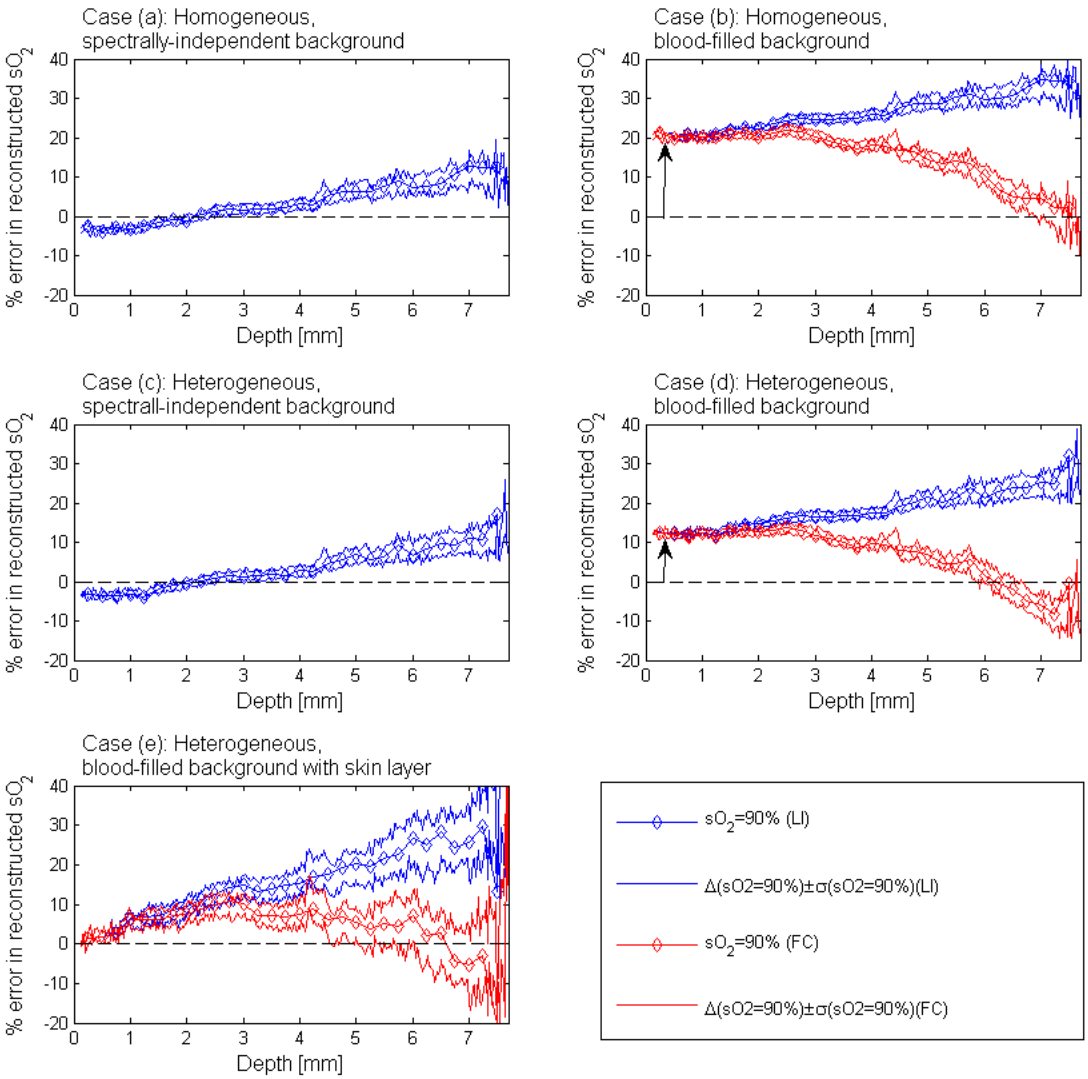

Figure 2. % error in sO_2 plotted as a function of vessel depth for phantom Cases (a)-(e) reconstructed using a *Type I* linear inversion (LI) and *Type II* fluence correction.

inversion worsening with increasing depth. For the spectrally-dependent background in Case (b), a similar trend is observed for the linear inversion; however, both the linear inversion and the fluence correction demonstrate significant error at superficial depths $\leq$1mm, indicated with the vertical black arrow in Figure 2(b). The 1D fluence correction performs identically to the linear inversion at superficial depths, due to the correction being small for small values of z, but improves the accuracy of the inversion dramatically at depths greater than 3mm. Similar observations can be made regarding Cases (c) and (d) where the background is heterogeneous, however the offset in the error in the reconstruction is significantly less for Case (d) than for Case (b), marked with a black vertical arrow in Figure 2(d). In Case (e), despite the presence of a skin layer, a lower error at all depths is observed, compared with Cases (b) and (d).

By comparing Cases (a) and (c) with Cases (b), (d) and (e) it is clear that the spectral colouring of the fluence is more marked in the presence of a spectrally-dependent absorbing background. However, contrasting Cases (b) with (d) and (e), illustrates that near the surface the difference in fluence at 680nm and 820nm is greater due to low absorption of back-scattered light. This is supported by the fact that the fluences at these two wavelengths in the first 0.85mm ($= 1/(\mu_a + \mu_s(1-g))$) in Case (b) are more than 5% higher than the fluences at the same

wavelengths for Case (d). The same analysis can be applied to Case (e) where the spectral impact of a skin layer is small, and the slightly lower offset error at the most superficial blood vessels is a result of the light already having been diffused by the highly scattering skin layer ($\mu_s = 21\text{mm}^{-1}$). Similar trends are observed when vessel oxygenation is 60%, 70%, 80% and 100%, although with larger standard deviation in the reconstruction error for lower values of vessel oxygenation. At 90% oxygenation, the higher accuracy yielded by both the linear inversion and the fluence correction in Case (d) relative to that achieved in Case (b) indicates that these approximate methods may be more useful when the tissue being imaged has a higher degree of vascularity.

The dynamic inversion technique classed in *Type I* was tested for Cases (d) and (e), but using an oxygenation change from 90% to 70%. The accuracy of this inversion approach was also examined in hypoxic conditions, whereby the background tissue oxygenation dropped by 60.7% to 50.7%, as well as in the presence of a skin layer. The results, plotted in Figure 3, show that the estimate of oxygenation in the vessel of interest is reconstructed accurately.

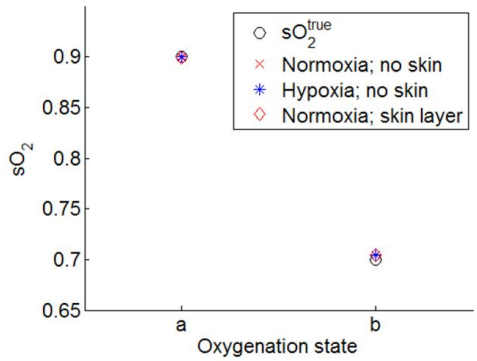

Figure 3. Reconstruction of sO_2 values in vessel of interest at oxygenation states a and b for normoxic and hypoxic background tissue conditions and in the presence of a skin layer. True oxygenation denoted by the black circles.

This demonstrates that the inversion algorithm performs well in all conditions, with hypoxia in the background tissue and the skin layer not negatively impacting results compared with normoxic conditions without a skin layer. The reason for the improved performance of this algorithm compared with the inversions tested above relies on the fact that the fluence at a single wavelength is not significantly affected by background oxygenation. Therefore, unlike the *Type I* linear inversion and *Type II* fluence correction, we expect the dynamic inversion to yield less accurate results when there are bulk changes in oxygenation, which is more likely to be the case in highly vascularised regions of tissue.

4.2 Acoustic Resolution Photoacoustic Microscopy

Numerical experiments were carried out in a confocal AR-PAM arrangement, whereby the light was weakly focused to a spot at depths of 0.625mm, 1.000mm and 1.500mm, with the acoustic focus at the same depths. The phantom was illuminated at 575nm and 590nm. MCX was again used to simulate the fluence and darkfield illumination was simulated by 25 pencil beam sources focused at the vessel of interest. This was confocal with a broadband, circular acoustic transducer (diameter 5mm), as shown in Figure 4. Assuming $\Gamma = 1$, propagation of the initial pressure distribution toward the detector at the tissue surface, in the presence of water coupling, was simulated using k-Wave.[12] The domain size was a cuboid 5mm by 5mm by 2mm and the maximum supported frequency of the acoustic grid was 200MHz. Synthetic focusing was applied to each element of the circular detector to introduce the necessary time delays for a 5mm diameter transducer in order to form an A-mode line, $p(\lambda, t)$.

The *Type I* and *Type II* inversions were applied to each of the five cases described in Section 2 for vessel oxygenation values of 70%, 80%, 90% and 100%. In the AR-PAM set-up, oxygen saturation was reconstructed at a single point in the blood vessel of interest at the focus position of the confocal arrangement. Figure 5 shows the accuracy of the linear and fluence corrected inversions for 90% vessel oxygenation as a function of depth for Cases (a)-(d).

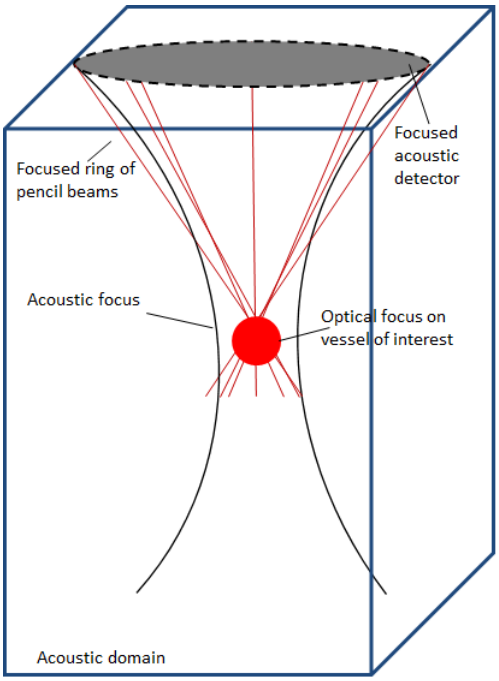

Figure 4. Schematic of confocal AR-PAM arrangement, showing focused pointwise pencil beam illumination and planar detector.

While at 0.625mm the linear inversion recovers oxygenation in the vessel to a high degree of accuracy in Cases (a) and (c), in which the background is spectrally-independent, a small degree of error is introduced through the spectral dependence of the background in Cases (b) and (d) (which unlike the previous cases, have a blood-filled background). Furthermore, it is clear that in these circumstances, the 1D fluence model in Equation (5) does not accurately model the fluence as it over-compensates at shallow depth. This may in part be due to the fact that darkfield illumination is used, resulting in a more complex fluence distribution at depths less than a few scattering mean-free-paths.

Both the linear inversion and the fluence correction demonstrate a percent error of greater than 20% in all cases for the 1mm and 1.5mm vessel depths, reflecting that the approximations used in each inversion scheme are no longer applicable. It is worth noting however that point-to-point variability in the fluence due to Monte Carlo noise may have also contributed to the poor accuracy of both algorithms in this configuration, although, unlike in the PAT simulations above, the focusing of light to a confined region mitigates against MC noise given the much higher fluences in the tissue afforded by focusing.

5. DISCUSSION

The phantoms used in this study to investigate the approximate inversion techniques are representative of the vast majority of scenarios that are encountered in PAI. For this reason, they would form a useful basis for testing a wide range of inversion algorithms, including full numerical inversion techniques. In this paper, the two approximate approaches tested were found to be accurate to within 10% of the true oxygenation value up to a depth of 2mm, in PAT, and 0.625mm, in AR-PAM, in the most realistic cases examined (Case (e) for PAT and Case (d) for AR-PAM). However, in applications where the background is likely to have low spectral-dependence, a linear inversion or fluence correction may provide accurate reconstruction of sO_2 as demonstrated above. The dynamic reconstruction method, which relies on the fluence being unchanged due to a change in vascular oxygenation, yields highly accurate results, even in the presence of a skin layer or hypoxic tissue conditions, and may be useful in a practical setting in brain activation or hypoxia studies.

When no *a priori* assumptions can be made regarding the background absorption, other inversion schemes may provide useful physiological information. For instance, principal component analysis and independent component

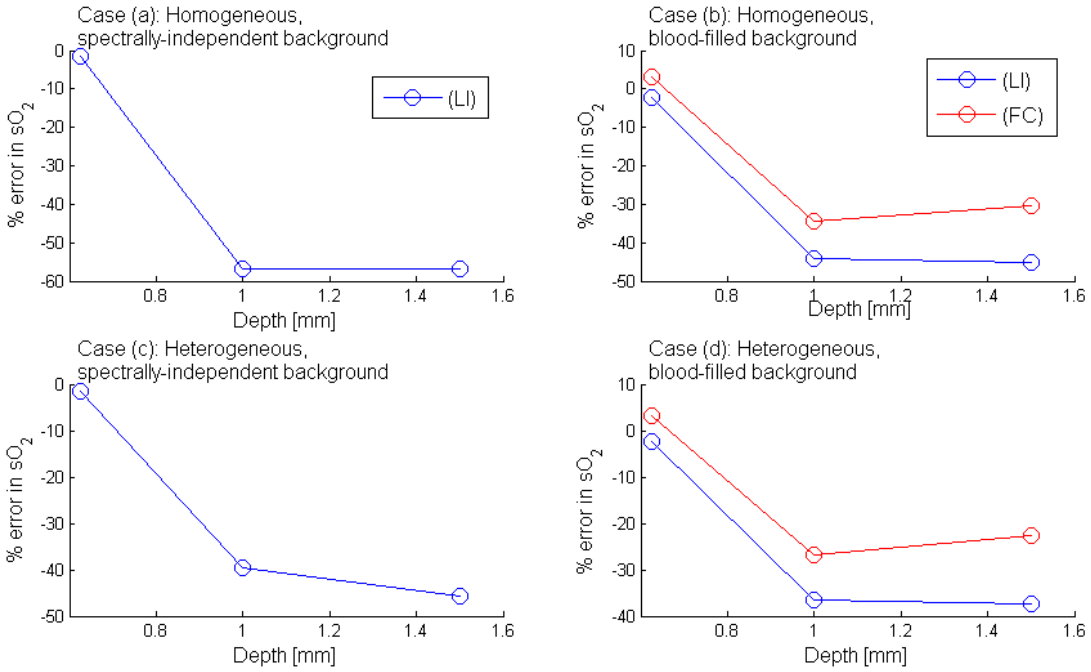

Figure 5. % error in sO_2 plotted as a function of vessel depth for phantom Cases (a)-(d) reconstructed using a *Type I* linear inversion (LI) and *Type II* fluence correction.

analysis can be employed in collaboration to identify spectrally distinct features in the image.[13] Rather than exploiting spectral properties of the image, exploitating the spatial characteristics of photoacoustic images has been attempted through the decomposition of the absorbed energy density into a low spatial frequency fluence term and a high spatial frequency absorption term.[14]

The above methods may be particularly useful when images contain artefacts and/or noise that show no dependence on the illumination wavelength. Throughout this paper it was assumed that perfect acoustic reconstruction was achieved for PAT, and the detector used for PAT was broadband. Acoustic detectors used in PAI have some bandwidth and will therefore be insensitive to frequencies outside this range. This introduces artefacts into images, therefore corrupting results obtained from the quantitative inversion. Furthermore, in PAT, it is rare that the object is imaged from all sides and, as such, limited-view artefacts are introduced into the image, making the inversion inaccurate in certain regions of the image.

6. CONCLUSIONS

In this paper, a numerical phantom study was conducted to assess the accuracy of two different inversion algorithms for the estimation of oxygen saturation in a vessel of interest in a mouse brain. Two classes of approximate inversion approach are examined; *Type I* methods assume the fluence is unchanged between the two excitation wavelengths, while *Type II* employs a simple, analytic fluence correction using known absorption coefficients of the background to reduce the impact of the spectral fluence colouring on the accuracy of the inversion. It was found that, although a linear inversion is accurate in superficial regions of the tissue, the accuracy of this approach decreases with increasing depth as the fluence becomes 'coloured' by the different absorbing structures within the tissue. A fluence correction tends to improve the accuracy of the inversion with increasing depth, particularly in PAT, while in AR-PAM, a fluence correction and a linear inversion perform similarly. It was found that dynamic reconstruction of oxygenation using a *Type I* method performs well, even during hypoxia. The limited accuracy of these approximate inversion schemes means they will only produce accurate values of oxygen saturation in few practical circumstances. Most notably, these approximate approaches are predominantly valid at shallow depth. In order to account for the spatial and spectral colouring of the fluence at depths greater than a few

mm, in PAT, and greater than several hundred microns, in PAM, a more accurate model of the fluence is required.

ACKNOWLEDGEMENTS

The mouse brain μCT data was kindly provided by Simon Walker-Samuel at the Centre for Advanced Biomedical Imaging, University College London.

REFERENCES

[1] Laufer, J., Delpy, D., Elwell, C., and Beard, P., "Quantitative spatially resolved measurement of tissue chromophore concentrations using photoacoustic spectroscopy : application to the measurement of blood oxygenation and haemoglobin concentration," *Physics in Medicine and Biology* **52**, 141–168 (2007).

[2] Sivaramakrishnan, M., Maslov, K., Zhang, H. F., Stoica, G., and Wang, L. V., "Limitations of quantitative photoacoustic measurements of blood oxygenation in small vessels.," *Physics in Medicine and Biology* **52**, 1349–61 (2007).

[3] Xia, J., Danielli, A., Liu, Y., Wang, L. L. V., and Maslov, K., "Calibration-free quantification of absolute oxygen saturation based on the dynamics of photoacoustic signals.," *Optics Letters* **38**, 2800–3 (2013).

[4] Bal, G. and Uhlmann, G., "Inverse diffusion theory of photoacoustics," *Inverse Problems* **26**, 085010 (2010).

[5] Laufer, J., Cox, B., Zhang, E., and Beard, P., "Quantitative determination of chromophore concentrations from 2D photoacoustic images using a nonlinear model-based inversion scheme.," *Applied Optics* **49**, 1219–33 (2010).

[6] Saratoon, T., Tarvainen, T., Cox, B. T., and Arridge, S. R., "A gradient-based method for quantitative photoacoustic tomography using the radiative transfer equation," *Inverse Problems* **29**, 1–19 (2013).

[7] Cox, B., Arridge, S., Köstli, K., and Beard, P., "Two-dimensional quantitative photoacoustic image reconstruction of absorption distributions in scattering media by use of a simple iterative method," *Applied Optics* **45**(8), 4 – 6 (2006).

[8] Yuan, Z., Wang, Q., and Jiang, H., "Reconstruction of optical absorption coefficient maps of heterogeneous media by photoacoustic tomography coupled with diffusion equation based regularized Newton method.," *Optics Express* **15**, 18076–81 (2007).

[9] Tarvainen, T., Cox, B. T., Kaipio, J. P., and Arridge, S. R., "Reconstructing absorption and scattering distributions in quantitative photoacoustic tomography," *Inverse Problems* **28**, 084009 (2012).

[10] Jacques, S. L., "Optical properties of biological tissues: a review.," *Physics in Medicine and Biology* **58**, R37–61 (2013).

[11] Fang, Q. and Boas, D. A., "Monte Carlo simulation of photon migration in 3D turbid media accelerated by graphics processing units," *Optics Express* **17**, 20178–90 (2009).

[12] Treeby, B. E. and Cox, B. T., "k-Wave: MATLAB toolbox for the simulation and reconstruction of photoacoustic wave fields.," *Journal of biomedical optics* **15**(2), 021314 (2010).

[13] Glatz, J., Deliolanis, N. C., Buehler, A., Razansky, D., and Ntziachristos, V., "Blind source unmixing in multi-spectral optoacoustic tomography.," *Optics Express* **19**, 3175–84 (2011).

[14] Rosenthal, A., Razansky, D., and Ntziachristos, V., "Quantitative optoacoustic signal extraction using sparse signal representation.," *IEEE Transactions on Medical Imaging* **28**, 1997–2006 (2009).